Defects enriched hollow porous Co-N-doped carbons embedded with ultrafine CoFe/Co nanoparticles as bifunctional oxygen electrocatalyst for rechargeable flexible solid zinc-air batteries

Zhao Lei[1,§], Yangyang Tan[1,§], Zeyi Zhang[1], Wei Wu[1], Niancai Cheng[1] (✉), Runzhe Chen[1], Shichun Mu[2] (✉), and Xueliang Sun[3] (✉)

[1] College of Materials Science and Engineering, Fuzhou University, Fuzhou 350108, China
[2] State Key Laboratory of Advanced Technology for Materials Synthesis and Processing, Wuhan University of Technology, Wuhan 430070 , China
[3] Department of Mechanical and Materials Engineering, The University of Western Ontario, London, ON N6A 5B9, Canada
[§] Zhao Lei and Yangyang Tan contributed equally to this work.

ABSTRACT

The construction and design of highly efficient and inexpensive bifunctional oxygen electrocatalysts substitute for noble-metal-based catalysts is highly desirable for the development of rechargeable Zn-air battery (ZAB). In this work, a bifunctional oxygen electrocatalysts of based on ultrafine CoFe alloy (4–5 nm) dispersed in defects enriched hollow porous Co-N-doped carbons, made by annealing SiO_2 coated zeolitic imidazolate framework-67 (ZIF-67) encapsulated Fe ions. The hollow porous structure not only exposed the active sites inside ZIF-67, but also provided efficient charge and mass transfer. The strong synergetic coupling among high-density CoFe alloys and Co-N$_x$ sites in Co, N-doped carbon species ensures high oxygen reduction reaction (ORR) and oxygen evolution reaction (OER) activity. First-principles simulations reveal that the synergistic promotion effect between CoFe alloy and Co-N site effectively reduced the formation energy of from O* to OH*. The optimized CoFe-Co@PNC exhibits outstanding electrocatalytic stability and activity with the overpotential of only 320 mV for OER at 10 mA·cm^{-2} and the half-wave potential of 0.887 V for ORR, outperforming that of most recent reported bifunctional electrocatalysts. A rechargeable ZAB constructed with CoFe-Co@PNC as the air cathode displays long-term cyclability for over 200 h and high power density (152.8 mW·cm^{-2}). Flexible solid-state ZAB with our CoFe-Co@PNC as the air cathode possesses a high open circuit potential (OCP) up to 1.46 V as well as good bending flexibility. This universal structure design provides an attractive and instructive model for the application of nanomaterials derived from MOF in the field of sustainable flexible energy applications device.

KEYWORDS

oxygen reduction reaction, ultrafine CoFe alloy, hollow porous carbons, zeolitic imidazolate framework-67, Zn-air battery

1   Introduction

Rechargeable Zn-air battery (ZAB) has been considered to be a promising next-generation energy conversion devices owing to its high specific energy density, low cost and high safety [1–4]. However, their commercialization are largely hindered by the sluggish kinetic behaviors and poor electrochemical stability of the air cathode materials, leading to the unsatisfactory rechargeability and low energy conversion efficiency [5]. Currently, Pt-based and Ru/Ir-based oxides catalysts have been developed to favor oxygen reduction reaction (ORR) and oxygen evolution reaction (OER), respectively. Unfortunately, the large-scale commercialization of ZAB was hampered by the high cost and limited supply of these noble metal-based catalysts [6–8]. Therefore, the development of earth-abundant and cost-effective noble-free metal electrocatalysts with excellent bifunctional performance is highly desirable to drive the commercialization of rechargeable ZAB [9–12].

In recent years, transitional metal and N Co-doped carbon-based nanohybrids (M-N-C, M= Co, Fe, Ni, Mn, etc.) system with highly active M-N$_x$ sites has attracted wide attention as the promising candidates for OER and ORR [13–17]. In particular, Co-N-C materials are extensively studied as effective oxygen electrocatalysts to improve the overall performance of ZABs [18–21]. Moreover, previous studies also displayed that the Co-based bimetallic, (e.g., CoFe, CoNi), N-doped carbon-based nanohybrids could further increase their catalytic activity and selectivity [22–27]. Therefore, the design of a multi-component Co-base hierarchy containing Co-N sites and Co-based alloy NPs may be an effective strategy as non-precious-metal electrocatalysts to promote the bifunctional ORR/OER activity [28–30].

Currently, cobalt-based metal-organic frameworks (MOFs), especially zeolite imidazole framework-67 (ZIF-67), has been widely used as suitable precursors to synthesize Co-N-C ORR/OER catalysts due to their three-dimensional adjustable porous structure, rich types of Co-N$_x$ active sites and high surface area [31–33]. However, the behavior of aggregation of

Co nanoparticles during pyrolysis not only reduces the active sites, but also results in poor dispersion of active sites and control over structural evolution, leading to significantly reducing their catalytic performance [34, 35]. More than that, inherent micropore-dominated structure and lengthy diffusion path of ZIF-67 derived carbon materials limit the diffusion of oxygen related species (O_2, H_2O and proton) to reach the internal active sites of carbon materials, which greatly reduces the utilization of active sites [36]. The strategies of the tuning the structure of MOF-derived Co-N-C catalytic materials were applied to overcome these limitations associated with ZIF-67 derived carbon materials and improve the electrocatalytic performance by maximizing mass transfer and exposing more active sites. Zhang et al. synthesized hierarchical porous Co, N co-doped carbon nanostructures with high ORR through pyrolyzing the mesoporous silicon oxide ($mSiO_2$) coated bimetallic (Zn and Co) ZIF precursor. Compared with the samples carbonized without coating SiO_2, the bimetallic ZIF-derived carbon materials with silicon coating showed better dispersion of metal nanoparticles, higher specific surface area, richer pore structure and higher ORR catalytic activity [36]. The studies of Mu and co-workers also showed that SiO_2 coating strategy could prevent the rapid aggregation of Co nanoparticles in the ZIF-67 during high-temperature pyrolysis, leading to the formation of small Co NPs with enhancing activity and inducing the catalytic growth of CNTs, thus obtaining good ORR catalytic activity [37]. Those studies suggest the coated MOF precursor with SiO_2 protective layer is an efficient method to improve the electrochemical activity of MOF derived Co-N-C catalytic materials through tuning the structure and favoring the mass transfer [34, 38, 39].

In this work, we have prepared defects enriched hollow porous Co-N-doped carbons embedded with ultrafine CoFe/Co nanoparticles (CoFe-Co@PNC) as highly active bifunctional oxygen electrocatalysts through annealing SiO_2 coated ZIF-67 encapsulated Fe ions. The coated silicon shell not only guarantee the formation of ultrafine CoFe/Co nanoparticles, but also favor the generation of hollow porous Co-N-doped carbon owing to its rigid structure counteracts the internal contraction during the carbonization process. The optimized CoFe-Co@PNC sample showed excellent bifunctional oxygen catalytic activity in alkaline electrolyte. In the practical application, the assembled rechargeable liquid Zn-air battery with our catalysts shows excellent performance and long-term cycling ability. Impressively, the corresponding rechargeable flexible solid-state ZAB also displays high open circuit voltage (1.46 V), excellent cycle stability and flexibility under different bending states, affording a promising application for future wearable electronics. This work provides new insights for the development of highly active bifunctional oxygen catalysts derived from MOF for sustainable flexible energy applications devices.

2 Experimental

2.1 Materials

All chemicals are from commercial and used without further purification. Cobalt nitrate hexahydrate ($Co(NO_3)_2 \cdot 6H_2O$, > 99.0%, Sinopharm Chemical Reagent Co., Ltd.); ferrous sulfate ($FeSO_4 \cdot H_2O$; > 99.0%, Sinopharm Chemical Reagent Co., Ltd.); 2-methyleimidazole (99.0%, Aladdin), methanol (99.5%, Sinopharm Chemical Reagent Co., Ltd.); ethanol (99.5%, Sinopharm Chemical Reagent Co., Ltd.). Ammonium hydroxide($NH_3 \cdot H_2O$; > 80 wt.%, Sinopharm Chemical Reagent Co., Ltd.); hydrofluoric acid (HF; > 40 wt.%, Sinopharm Chemical Reagent Co., Ltd.) and potassium hydroxide (KOH,

85%, Sinopharm Chemical Reagent Co., Ltd.), Pt/C (Johnson Matthey, 20%), RuO_2 (Macklin) and de-ionized water with the specific resistance of 18.25 $M\Omega \cdot cm^{-1}$ (obtained by reversed osmosis followed by ion-exchange and filtration).

2.2 Preparation methods

ZIF-67: In a typical experiment, 6.15 g $Co(NO_3)_2 \cdot 6H_2O$ and 6.787 g 2-MeIM was added to 200 mL methanol with string for 15 min respectively. Then, above two solutions were mixed for 2 h at room temperature with string. The resulting purple precipitates were collected by centrifugation at 6,500 rpm for 10 min and washed with methanol several times. The resulting sample was dried in a vacuum at 80 °C overnight.

ZIF-67@SiO₂@Fe: 200 mg of ZIF-67 and 0.8 mL $NH_3 \cdot H_2O$ was dispersed in 160 mL of methanol by ultrasonication. Then 0.8 mL tetraethyl orthosilicate (TEOS) was dissolved and string 8 h, washed with methanol several times and dried under vacuum at 70 °C overnight. The resulting $ZIF-67@SiO_2$ was added into a mixed solution of 100 mL of ethanol, 80 mg $FeSO_4 \cdot H_2O$ and dispersed by sonication, followed by rotary evaporation. The dried sample was subjected to pyrolysis under a flowing N_2 atmosphere at 700 °C for 2 h with a heating ramp rate of 5 °C·min^{-1}.

CoFe-Co@PNC: The SiO_2 shell of $ZIF-67@SiO_2@Fe$ was etched out in HF solution(4 wt.%) for 6, 12, 24 h. the pre-leached catalyst was calcined for the second time at 800 °C under an N_2 atmosphere to afford the final CoFe-Co@PNC-6, 12, 24 catalyst.

2.3 Characterizations

The electrochemical workstation (Autolab) with a three-electrode system was used for the ORR and OER tests at room temperature, respectively. The platinum sheet and Ag/AgCl electrode were utilized as the counter and reference electrodes, respectively. The working electrode is the as-prepared catalysts coated with a glassy carbon electrode. The electrolyte are O_2 saturated 0.1 M KOH (ORR) and 1 M KOH (OER). The catalyst ink was prepared by blending the catalyst powder (5 mg) with 30 μL Nafion solution (5 wt.%) and 970 μL of the mixed solution (deionized water/isopropanol = 1:1) in an ultrasonic bath. 10 μL of catalyst ink was then pipetted onto the GC surface, leading to a catalyst loading of 0.25 mg·cm^{-2}. Commercial 20 wt.% Pt/C and RuO_2 was measured for comparison (0.1 mg·cm^{-2}). The applied potentials were normalized by using the reversible hydrogen electrode (RHE) according to the Eq. (1)

$$E_{(RHE)} = E_{(Ag/AgCl)} + 0.197 + 0.059pH \tag{1}$$

The overall electron transfer numbers per oxygen molecule involved in a typical ORR process can be calculated from the slopes of Koutecky–Levich (K–L) plots using the following Eq. (2)

$$1/j = 1/j_k + 1/B\omega^{1/2} \tag{2}$$

where j_k is the kinetic current at a constant potential and ω represents the electrode rotating speed. B can be determined from the slope of the K–L plots based on Levich equation

$$B = 0.2nF(D_{O_2})^{2/3}v^{-1}/6C_{O_2} \tag{3}$$

where n represents the transferred electron number per oxygen molecule, F is Faraday constant (96,485 C·mol^{-1}), D_{O_2} is the diffusion coefficient of O_2 (1.9×10^{-5} $cm^2 \cdot s^{-1}$), v is the kinetic viscosity ($v = 0.01$ $cm^2 \cdot s^{-1}$) and C_{O_2} is the bulk concentration of O_2 (1.2×10^{-6} mol·cm^{-3}). When expressing the rotation speed in rpm, the constant 0.2 is applied.

In Tafel plot, the kinetic current was calculated from the

mass-transport correction of rotating disk electrode (RDE) data by the followed Eq. (4)

$$j_k = (j \times j_L)/(j_L - j) \qquad (4)$$

where j is the current density and j_L is the limiting current density. Rotating ring disk electrode (RRDE) technique was also employed to determine the reaction pathway (electron transfer number) for ORR by detecting the HO_2^- formation, in which the ring potential was held constantly at 1.50 V vs. RHE. The disk electrode was scanned at a rate of 10 mV·s⁻¹ with a rotation rate of 1,600 rpm. The electron transfer number (n) was determined by the followed equation

$$n = 4I_d/(I_d + I_r/N) \qquad (5)$$

$$HO_2^-\% = 200I_r/N(I_d + I_r/N) \qquad (6)$$

where I_d is disk current, I_r is ring current, and N is the current collection efficiency.

2.4 Theoretical calculations

All the calculations, which performed within density functional theory (DFT) framework, were implemented with Vienna *ab-initio* simulation package (VASP). The Projector-Augmented Wave (PAW) potentials' database was used to simulate the relation between valence electrons and cores, while the Perdew-Burke-Ernzerh (PBE) of exchange correlational function and the generalized-gradient approximation (GGA) was adopted to investigate the transfer and association of electrons. In order to investigate the charge density distribution near the active site exposed on the surface of the CoFe-N-C model and to demonstrate the optimization and contribution of Fe, the charge transfer was calculated by subtracting the charge density of isolated active site (Co-N₄) and the charge density of isolated CoFe-N-C without active site from the charge density of the CoFe-N-C. The same principle applies to the Co-N-C model. The detailed calculations are shown in the ESM.

2.5 Fabrication of primary Zn-air battery

Liquid zinc–air battery assembly. The anode and the air cathode electrode were the zinc plate and a hydrophobic carbon paper with a gas diffusion layer covered with the electrocatalysts (the effective catalyst area is 0.785 cm⁻²), respectively. The homogeneous catalyst ink was obtained through mixing the electrocatalyst (10 mg), acetylene black (1.0 mg), and 30 μL of Nafion solution (5%, DuPont) in 1 mL of the mixed solution (deionized water/ethanol = 1:1). For comparison, noble metal catalysts (Pt/C and RuO₂), the loading is 0.2 mg·cm⁻². The alkali electrolyte was constituted of KOH (6 M) and Zn(CH₃OO)₂ (0.2 M).

Flexible solid-state Zn–air battery assembly. A polished zinc foil (0.08 mm thickness) was used as anode. The air electrode was made by dropping a certain volume of catalyst ink onto a cleaned nickel foam substrate (1 cm × 3 cm) with a catalyst loading of 0.50 mg·cm⁻². The gel polymer electrolyte was prepared as follows: 10.0 g polyvinyl alcohol (PVA) powder (M_W 19,500, Aladdin) was dissolved in 100.0 mL deionized water at 85 °C under magnetic stirring for 2.0 h. Then 10.0 mL of 6.0 M KOH filled with 0.20 M Zn(CH₃OO)₂ was added and the electrolyte solution was kept stirring at 85 °C for 1.0 h. Then the solution was frozen at −3 °C over 12 h, and then thawed at room temperature. Then the flexible solid-state Zn-air battery was assembled with air electrode and zinc foil placed on the two sides of PVA gel, and PI film is used to seal the sandwich structure of nickel foam-PVA-zinc foil.

3 Results and discussion

3.1 Synthesis and structure characterization

The synthesis process of defects enriched hollow porous Co-N-doped carbons embedded with ultrafine CoFe/Co nanoparticles (NPs) is illustrated in Scheme 1. Firstly, ZIF-67 precursor with a typical polyhedral morphology of about 1 μm was synthesized, and then mesoporous SiO₂ shell was uniformly coated on the outer layer of ZIF-67 precursor by hydrolysis of TEOS. As shown in Figs. S1 and S2 in the Electronic Supplementary Material (ESM), compared with the smooth surface of pure ZIF-67 precursor, the surface of ZIF-67 coated with SiO₂ becomes rough and uneven, indicating that SiO₂ shell is successfully coated on the ZIF-67 precursor. Subsequently, the Fe ions easily pass through amorphous silicon layer and incorporated into the pores/cavities of as-prepared ZIF-67 precursors coated with SiO₂ (Fe@ZIF-67@SiO₂) [40]. Finally, a CoFe-Co@PNC was obtained through annealing Fe@ZIF-67@SiO₂ nanocomposites, followed by HF acid etching and subsequent secondary high temperature treatment. The detailed morphology of CoFe-Co@PNC is characterized by scanning electron microscopy (SEM) and transmission electron microscopy (TEM). The hollow porous carbons were observed (Figs. 1(b)–1(d), and Fig. S3 in the ESM) after HF acid etching of annealing Fe@ZIF-67@SiO₂ nanocomposites as shown in Fig. 1(a) and Fig. S4 in the ESM, which basically maintained the frame structure of ZIF-67. With the increase of HF acid etching time, the hole on carbon shell of CoFe-Co@PNC gradually increases due to the removal of the coated SiO₂ shell and the corrosion damage of strong acid on carbon network. The mapping in Fig. S5 in the ESM shows that there exist SiO₂ for 6 h HF acid etching of CoFe-Co@PNC samples (CoFe-Co@PNC-6), while the signal of SiO₂ disappeared for CoFe-Co@PNC-12 (Fig. S6 in the ESM) and CoFe-Co@PNC-24
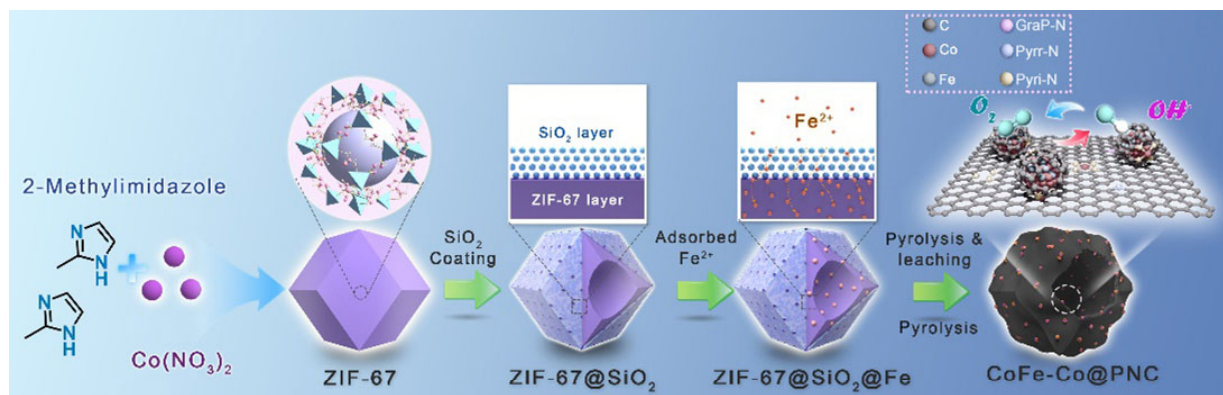
Scheme 1 Illustration of the preparation process of the CoFe-Co@PNC catalysts.
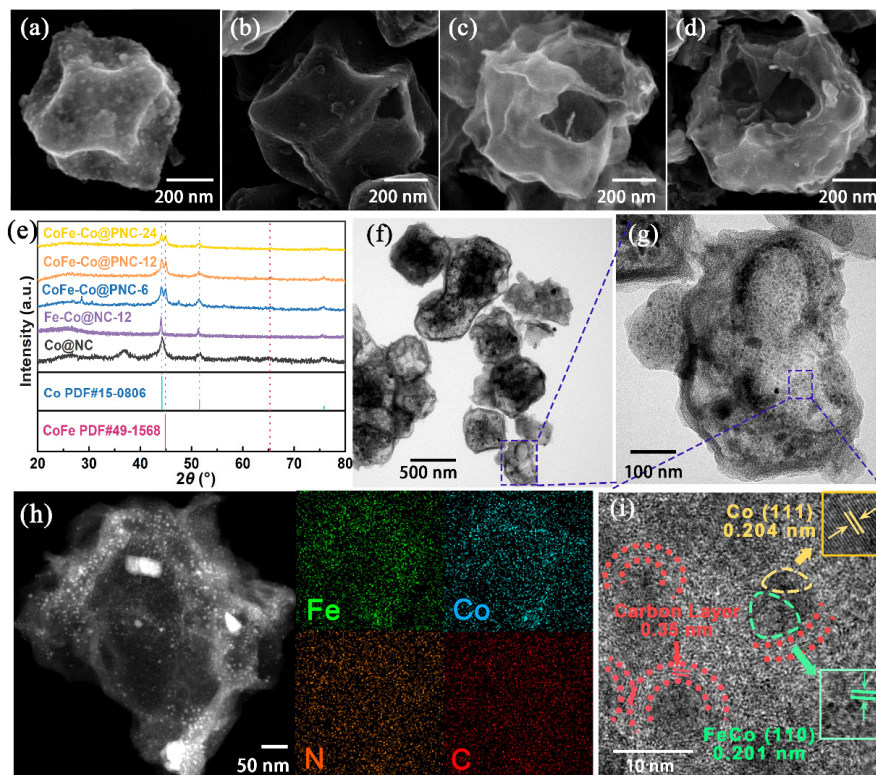
Figure 1 SEM images of (a) ZIF-67@SiO₂@Fe, (b) CoFe-Co@NPC-6, (c) CoFe-Co@NPC-12, and (d) CoFe-Co@NPC-24. (e) XRD patterns of Co@NC, Fe-Co@NC-12, CoFe-Co@NPC-6, CoFe-Co@NPC-12 and CoFe-Co@NPC-24. (f) and (g) TEM, (i) HR-TEM image and (h) STEM and the corresponding elemental mappings of Fe, Co, N, and C of CoFe-Co@NPC-12.

(Fig. S7 in the ESM). This result suggests that the SiO₂ shell was removed after 12 h HF acid etching. The formation of hole on hollow structure carbons without the SiO₂ shell is favorable for exposing the active sites inside of carbon shell and facilitating the rapid mass transport. X-ray diffraction (XRD) pattern in Fig. 1(e) shows that the CoFe-Co@PNC catalysts possess multiphase NPs consist of CoFe and Co NPs. The intensities of diffraction of multiphase NPs are similar for CoFe-Co@PNC-6 and CoFe-Co@PNC-12. When the HF acid etching time increases to 24 h, the intensity of diffraction of multiphase NPs decreases because the dissolution of multiphase NPs caused by the corrosion of HF acid, which leads to low activity. TEM images of CoFe-Co@PNC-12 display hollow structure with abundant uniformly dispersed metal nanoparticles (Figs. 1(f) and 1(g)). It is worth noting that the Co-Fe@NC-12 derived from ZIF-67 encapsulated Fe ions without SiO₂ coating does not show a hollow structure in Fig. S8 in the ESM, indicating the SiO₂ layer contributes to the formation of the hollow structure because its rigid structure counteracts the internal contraction in the carbonization process of ZIF@mSiO₂ [41]. That's the carbonization process preferentially occurs at the interface between the mSiO₂ layer and ZIF-67 due to the temperature difference, and then the remaining MOFs shrink outward during the carbonization process, resulting in the formation of a hollow cavity structure with mesoporous walls after HF acid etching. The high-resolution TEM (HRTEM) image demonstrates (Fig. 1(i)) that the size of NPs are about 5 nm in diameter. The lattice spacing measurement shows that these NPs consist of the (110) facets of CoFe (JCPDS No. 49-5168) and the (111) facets of Co (JCPDS No. 15-0806) which is in good agreement with XRD result. In addition, the local high-angle annular dark-field-scanning transmission election microscope (HAADF-STEM) images and the corresponding X-ray energy dispersive spectroscopy (EDS) element mappings

and line scans of CoFe-Co@PNC-12 in Figs. S9 and S10 in the ESM also further confirmed the formation of CoFe alloy nanoparticles. More importantly, these multiphase NPs were embedded in disordered graphite carbons (Fig. S11 in the ESM), which is beneficial to enhancing electrocatalytic activity due to more exposed active sites [42]. In Raman spectra (Fig. S12 in the ESM), with the increase of etching time, the ratio of D to G-band (I_D/I_G) of the sample increases gradually due to the corrosion of HF acid, in according with the SEM results. In addition, the ratio of I_D/I_G of CoFe-Co@PNC are greater than that of ZIF-67 derived porous carbons, indicating our strategy in this work can increase the defect degree of sample, conducive to the formation of more active sites [43, 44]. EDS element mapping (Fig. 1(h)) further reveals that, Co, Fe, N and C elements are distributed in the whole structure, especially Fe and Co elements have the same distribution region.

The pore properties and surface areas of obtained electrocatalysts were investigated by the N₂ adsorption/desorption measurements (Fig. 2(a)). Compared with the direct carbonization ZIF-67, CoFe-Co@PNC obtained through SiO₂ coated ZIF-67 and then encapsulated Fe ions has a significantly increased uptake in the relatively low N₂ pressure (P/P_0 = 0–0.015) and a larger range of the hysteresis loop in the high N₂ pressure (P/P_0 = 0.4–0.95), indicating significant increase in the micropore and the mesopore for CoFe-Co@PNC. Notably, the pore size distribution diagram inset shows that CoFe-Co@PNC-12 possesses higher micropores and mesopores at 0.43 and 3.98 nm, respectively. In addition, CoFe-Co@PNC-12 also has the highest the specific surface area (564 m²·g⁻¹) and total pore volume (0.70 cm³·g⁻¹), much higher than ZIF-67 derivatives (293 m²·g⁻¹ and 0.19 cm³·g⁻¹), CoFe-Co@PNC-6 (385 m²·g⁻¹ and 0.32 cm³·g⁻¹) and CoFe-Co@PNC-24 (486 m²·g⁻¹ and 0.64 cm³·g⁻¹) which are mainly attributed to the relatively unique hollow structure of CoFe-Co@PNC-12. Detailed data
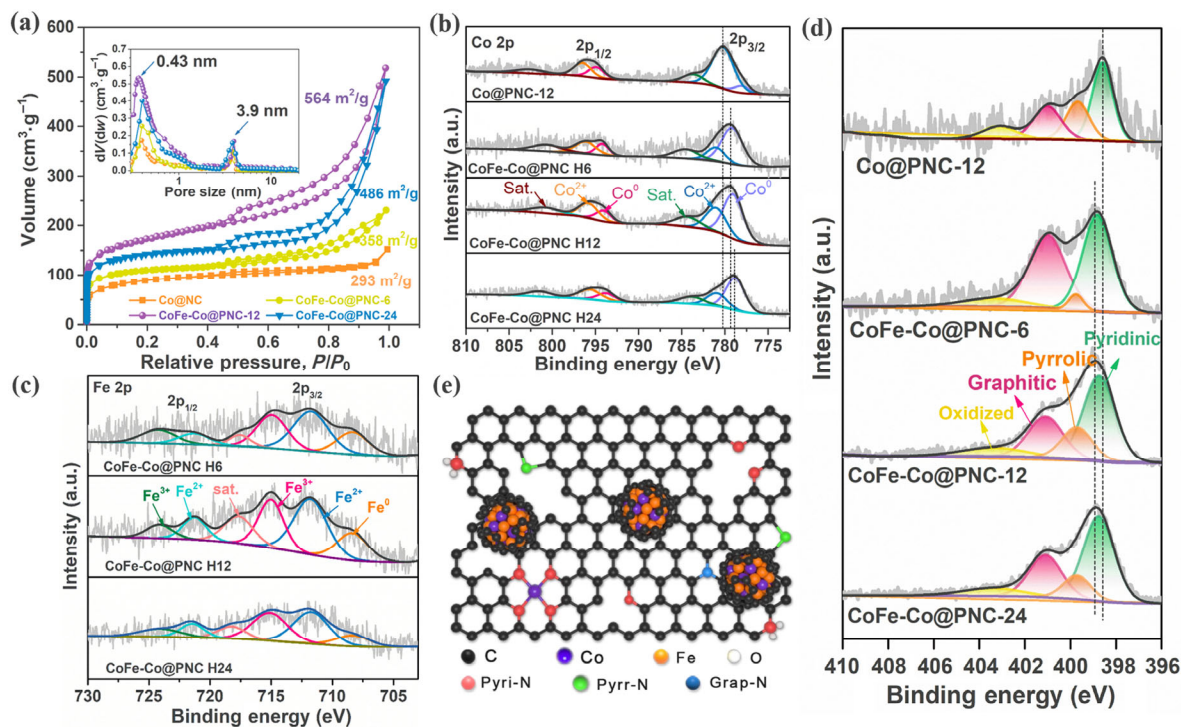
Figure 2 (a) N_2 adsorption-desorption isotherms of Co@NC, CoFe-Co@PNC-6, CoFe-Co@PNC-12 and CoFe-Co@PNC-24, inset figure illustrates the pore size distributions; HR-XPS spectrum of (b) Co 2p, (c) Fe 2p and (d) N 1s of CoFe-Co@PNC-6, FeCo-Co@PNC-12 and FeCo-Co@PNC-24. (e) Schematic diagram of the existence of each element in FeCo-Co@PNC-12.

of surface area and pore properties of CoFe-Co@PNC and ZIF-67 derivatives are shown in Table S1 in the ESM. The large surface area with high porosity are the key properties of porous carbon catalysts achieving good activity. These data suggest that the annealing SiO_2 coated ZIF-67 encapsulated Fe ions is an efficient strategy to synthesize hollow porous carbons with excellent hierarchical pores, resulting in the increase in the activity by affording more exposed active sites and improving the mass transfer ability.

The surface chemical composition of the samples was monitored by X-ray photoelectron spectroscopy (XPS). The existence of Co, Fe, N, O and C elements in CoFe-Co@PNC-12 catalysts were verified by the survey spectrum (Fig. S13 in the ESM). Detailed element content data are presented in Table S2 in the ESM. Compared with other samples, the CoFe-Co@PNC-12 obtained by HF acid etching for 12 h contained the highest Co (1.78 at.%), Fe (0.42 at.%) and N (7.6 at.%) contents (Fig. S14(a) in the ESM). Namely, with the increase of HF acid etching time, the contents of Co, Fe and N elements of the obtained sample showed a trend of first increasing and then decreasing. This may be attributed to the existence of silicon shell on CoFe-Co@PNC-6 and the excessive corrosion of HF acid etching on CoFe-Co@PNC-24. The high resolution Co 2p fitting peaks spectrum (Fig. 2(b)) shows zerovalent cobalt located at 779.1 and 793.9 eV and the peaks at 781.6 and 796.4 eV related to ionic state of cobalt with apparent satellites (785.2 and 802.7 eV), resulting from CoFe-Co NPs and Co-N species [45, 46]. The Fe 2p high resolution spectrum in Fig. 2(c) also shows the peaks at 707.4 and 720.1 eV, related to Fe with zero-valence state, suggesting metallic Fe in CoFe alloys [47]. These results indicate that the addition of Fe atoms successfully formed highly active CoFe alloy nanoparticles and introduced them into the defects enriched hollow porous Co, N co-doped carbon. In addition, due to the exact removal of the silicon layer, CoFe-Co@PNC-12 contains more CoFe alloys and Co-N_x content than CoFe-Co@PNC-6 and

CoFe-Co@PNC-24 (Fig. S14(b) in the ESM), which means more highly active oxygen catalytic sites, indicating that Co is not only alloying with Fe, but also coordinating with nitrogen atoms in the carbon network to form the Co-N_x site. Compared with Co@PNC-12, the Co^0 peak of CoFe-Co@PNC was significantly larger, and the ionic state Co peak was weaker (Fig. 2(b)), indicating that the introduction of Fe atom changed the Co atom coordination environment through the formation of CoFe alloy. Furthermore, clear negatively shifted in the binding energy of the Co 2p peak and positively shifted in the binding energy of N 1s peak of CoFe-Co@PNC compared to Co@PNC-12 are observed (Figs. 2(b) and 2(d)), which further indicated that the formation of CoFe alloy weakened the coordination between Co atom and N atom, so that the electrons around N atoms were transported. These analyses demonstrates that the strong coupling between bimetal FeCo alloy and defects enriched Co, N-doped carbon through the metal-N coordination, which are expected as the main ORR/OER active site to accelerate the oxygen catalytic process by optimizing the local charge structure. In addition, it is well known that the N contents and the different N-based active sites in the carbon matrix play a vital role in achieving high electrocatalytic activity [48, 49]. The high-resolution N 1s spectrum displays the existence of pyridine N (398.6 eV), pyrrolic N (399.7 eV), graphitic N (401.2 eV) and oxide N (403.6 eV) (Fig. 2(d)) [50, 51]. In addition, as a widely recognized electrochemical active site, the pyridinic N species can make the neighboring sp^2-bonded C atoms have a relatively high positive charge density, thus promoting the adsorption of reactants (such as O_2, OH^-) and promoting the electron transfer at interface of catalyst surfaces [52, 53]. Based on the above analysis, a possible existence structure of each element in CoFe-Co@PNC-12 as shown in Fig. 2(e).

3.2 ORR and OER catalytic activity

The ORR activities of the CoFe-Co@PNC catalysts together

with commercial Pt/C as comparison were firstly explored by measuring cyclic voltammogram (CV) in O₂-saturated 0.1 M KOH media. Compared with other catalysts, CoFe-Co@PNC-12 shows a more positive O₂ reduction peak at ≈ 0.83 V (Fig. S15 in the ESM). The linear sweep voltammetry (LSV) curves also show that CoFe-Co@PNC-12 has higher ORR activity than that of CoFe-Co@PNC-6, CoFe-Co@PNC-24 and Co@NC. These results suggest that the tuning the structure of MOF-derived carbon nanomaterials is beneficial to determining the ORR activity. More importantly, CoFe-Co@PNC-12 possesses a half-wave potential ($E_{1/2}$) of 0.89 V with an onset potential (E_{onset}) of ≈ 1.03 V, better than those of Pt/C ($E_{1/2}$ = 0.88 V, E_{onset} = 1.01 V) and most recently reported Co-based ORR catalysts (Table S4 in the ESM). The excellent ORR catalytic activity of CoFe-Co@PNC-12 was further verified by the Tafel curve and electrochemical impedance spectroscopy (EIS). As shown in Fig. 3(b) and Fig. S16(c) in the ESM, compared with other catalysts, the CoFe-Co@PNC-12 achieving a lower Tafel slope value (61 mV·dec⁻¹) and the smaller charge transfer resistance, demonstrating the design of hollow porous Co-N-doped carbons embedded with ultrafine CoFe/Co NPs using our strategy can improve the ORR kinetics. The average electron transfer number per O₂ for CoFe-Co@PNC-12 according to the corresponding Koutecky–Levich (K–L) plots is estimated to be about 3.98 (Figs. S16(a) and S16(b) in the ESM), indicating that CoFe-Co@PNC-12 favor ORR through a direct four-electron pathway at relatively low overpotentials [6, 54]. To further

determine the ORR path, a RRDE technology is also performed to evaluate the generation of peroxide (HO₂⁻) at different potentials (Fig. S16(d) in the ESM). The electron yield of HO₂⁻ is between 0.6% and 1.6% for CoFe-Co@PNC-12, and the corresponding electron transfer number n is between 3.99 and 3.96, indicating that the reduction sample has high four-electron path selectivity [55, 56]. In addition, as shown in Figs. S17 and S18 in the ESM, CoFe-Co@PNC-12 has a higher oxygen catalytic activity than Co-Fe@NC-12 derived from ZIF-67 encapsulated Fe ions without SiO₂ coating and Co@PNC-12 derived from the silicon-coated ZIF-67 without permeation Fe²⁺, indicating that silicon protection strategy and iron infiltration can improve the catalytic activity of the catalyst, which further confirms that the CoFe alloy is the main contribution to the great improvement of ORR and OER catalytic performance. Stability is another key factor in practical applications. As shown in Fig. 3(c), the half-wave potential of CoFe-Co@PNC-12 has almost no shift after 5,000 cycles, while it negatively shifts about 35 mV for Pt/C, which shows that our catalyst has excellent durability in alkaline medium. In addition, in comparison with the commercial Pt/C catalyst, CoFe-Co@PNC-12 also showed higher tolerance to the methanol cross-over effect in alkaline solution (Figs. S16(e) and S16(f) in the ESM).

The OER performance of all electrocatalysts are investigated by LSV curves as shown in Fig. 3(d). The CoFe-Co@PNC-12 achieves a potential ($E_{j=10}$) of 1.55 V at a current density of
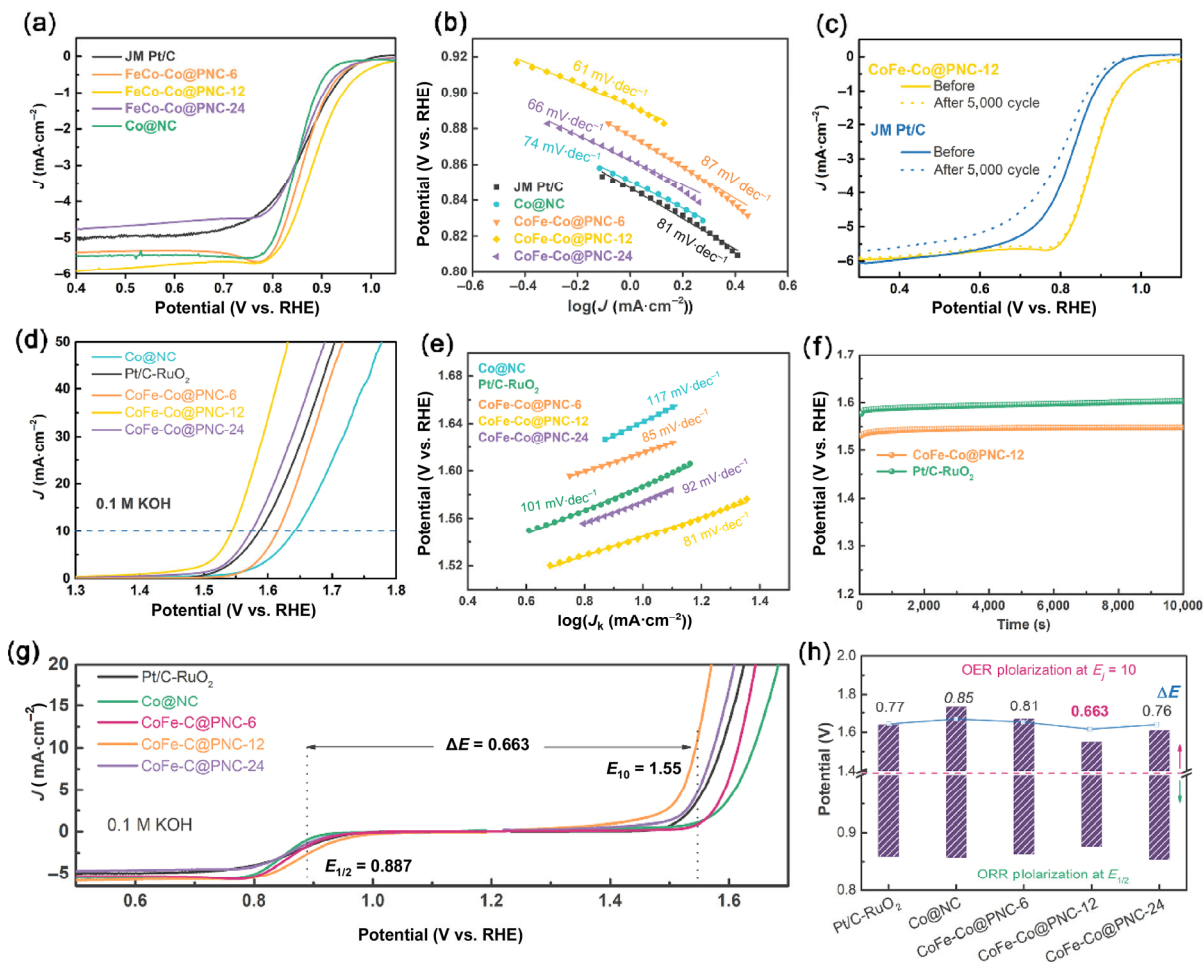

Figure 3 (a) ORR curves and (b) corresponding Tafel plots of various catalysts in O₂-saturated 0.1 M KOH solution at 1,600 rpm (scan rate: 10 mV·s⁻¹). (c) LSV curves of the CoFe-Co@PNC-12 and 20% Pt/C catalyst before and after 5,000 cycles for the ORR. (d) OER curves and (e) Tafel plots of various catalysts at 1,600 rpm in O₂-saturated 0.1 M KOH electrolyte. (f) Chronopotentiontiometric curves of CoFe-Co@PNC-12 and RuO₂ at current density of 10 mA·cm⁻². (g) LSV curves of Co@NC, CoFe-Co@PNC-6, CoFe-Co@PNC-12, CoFe-Co@PNC-24 and Pt/C-RuO₂ catalysts in the full OER/ORR region, and (h) Corresponding value of ΔE (ΔE = $E_{j=10}$ − $E_{1/2}$).

10 mA·cm^{-2}, which compares favorably to other catalysts and commercial RuO$_2$ ($E_{j=10}$ = 1.59 V). In addition, CoFe-Co@PNC-12 also shows the largest OER current density with fastest current density increasing in the whole potential window, which further revealed the outstanding OER activity. It is worth mentioning that the CoFe-Co@PNC displays an obvious lower potential at 10 mA·cm^{-2} than Co@NC, which further proves that the introduction of Fe contributes significantly to the enhancement of OER activity. Moreover, FeCo-Co@PNC-12 also displays a much lower Tafel slope (82 mV·dec^{-1}) than other catalysts and RuO$_2$ (83 mV·dec^{-1}), indicating that hollow porous Co-N-doped carbons embedded with ultrafine FeCo/Co NPs promoted OER kinetics. The double layer capacitance (C_{dl}) derived from electrochemical active area (ECSA) was also applied to evaluate the OER catalytic activity of as-prepared catalyst by calculating CV curves with different scan rates from 10 to 100 mV·s^{-1}. Figure S19 in the ESM shows that CoFe-Co@PNC-12 has a higher C_{dl} value (30.5 mF·cm^{-2}) than other catalysts, indicating that this catalyst has larger ECSA, which can expose more Co-based active sites (CoFe alloy and Co-N$_x$), and improve the transfer rate of oxygen-containing intermediates, thereby improving OER reaction activity and kinetics. In addition, as shown in Fig. S19(f) in the ESM, the TOF$_{Co+Fe}$ value of CoFe-Co@PNC-12 catalyst was 0.115 s^{-1}, which was much higher than Co@NC (0.006 s^{-1}) derived from pure ZIF-67, indicating that CoFe-Co@PNC-12 contains more catalytic active sites than Co@NC. Importantly, as shown in Fig. S20 in the ESM, through the correlation specific surface area and ORR/OER parameters, it can be found that the ORR/OER performance of obtained catalyst is positively related to its specific surface area, especially the ECSA data of catalyst, which again indicates that the large specific surface area brought by hollow structures can enhance ORR/OER catalytic activity. In order to verify the bifunctional catalytic activity of CoFe-Co@PNC-12, the potential difference ΔE between $E_{1/2}$ for ORR and $E_{j=10}$ for OER was evaluated (Fig. 3(g)), and a smallest value ΔE ($\Delta E = E_{j=10} - E_{1/2}$) implies superior bifunctional catalytic activity [57]. It can be seen in Fig. 3(h) that CoFe-Co@PNC-12 has the lowest ΔE of 0.663 V, smaller than other as-prepared CoFe-Co@PNC catalysts, Pt/C-RuO$_2$ and most recently reported catalysts (Table S5 in the ESM), suggesting the outstanding bifunctional electrochemical activity. Furthermore, as shown in Fig. S21 in the ESM, a pyrolysis temperature gradient examination (600, 700, 800 and 900 °C) showed that the CoFe-Co@PNC-12 obtained at 800 °C had the highest ORR/OER catalytic activity, due to the formation of small-size CoFe alloy nanoparticles at 800 °C pyrolysis temperature.

In view of the above analysis, the outstanding bifunctional oxygen catalytic activity of CoFe-Co@PNC-12 catalyst could be attributed to the unique structure of defects enriched hollow porous Co-N-doped carbons embedded with ultrafine CoFe-Co nanoparticles. The SiO$_2$ coating plays a vital role in the construction of this unique structure, confirmed by the above analysis. The coating of rigid silicon shell not only effectively generate ultrafine CoFe-Co embedded in porous Co-N-doped carbons, preventing the agglomeration growth of Fe and Co particles, but also promotes the formation of hollow porous Co-N-doped carbons with numerous hierarchical pores thus exposing more active sites and accelerating the mass transfer efficiency.

3.3 Catalytic mechanism and DFT calculations

To further theoretically elucidate the synergistic effect of CoFe alloy and Co-N site for enhancing catalytic efficiency, we carried out DFT calculations to reveal the ORR/OER mechanism of CoFe-Co@PNC-12 and the Co/Co-NC without Fe. As shown in the Fig. S22 in the ESM, the two models of Co@Co-NC and CoFe@Co-NC were constructed, respectively, by constructing Co NPs and CoFe NPs embedded in the carbon network with Co-N$_4$. The optimized adsorption configurations of oxygen intermediates (O*, OOH* and OH*) adsorbed on CoFe-Co@PNC-12 are shown in Fig. 4(a). In our DFT, both ORR and OER typically undergo four elementary steps in alkaline media; whereas the ORR proceeds through the formation of HOO*, O*and HO*, and the OER occurs in the reverse direction [58, 59]. For ORR catalysis, under the ideal environment of equilibrium potential of 1.23 V and pH of 0 (Fig. 4(b)), the HO*desorption is the rate-determining step (RDS) with 0.72 eV barrier energy for Co/Co-NC, whereas the barrier energy decreases to 0.39 eV for CoFe@Co-NC in the desorption process of HO*(RDS). Regarding the OER, the RDS for CoFe@Co-NC and Co/Co-NC is the oxidation process from HO* to O*. Therefore, the RDS energy values are calculated to be 0.5 V for CoFe@Co-NC, much lower than 1.12 V for Co/Co-NC, indicating OER reaction is more likely to occur in CoFe@Co-NC due to the smaller energy barrier. The total densities of states (DOS) diagram in Fig. 4(c) shows that the energy of Co in CoFe alloy at Fermi level of 0 is weaker than pure Co, indicating the charge distribution of Co is optimized to be more favorable for the adsorption and desorption of oxygen species due to the charge transfer with Co-N site. The charge density distribution in Fig. 4(d) also shows a higher charge density at the Co-N central site of CoFe@Co-NC compared with Co/Co-N$_4$ (Fig. 4(e)), which clearly confirms the obvious interface electron transfer from CoFe to Co-N$_4$. Therefore, benefitting from the atomic engineering of CoFe@Co-NC with double active sites between CoFe alloy and Co-N$_4$, the adsorption and desorption of intermediates O*and HO* on Co
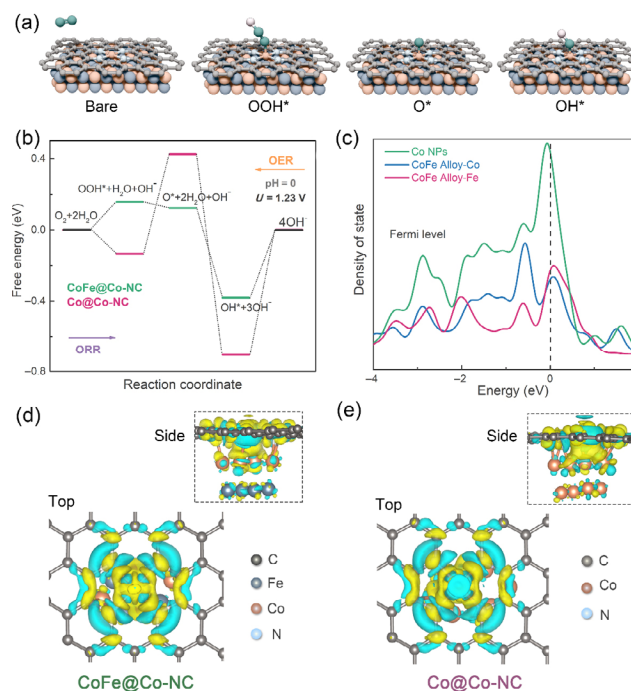

Figure 4 (a) The optimized adsorption configurations of oxygen intermediates (O*, OOH* and OH*) adsorbed on CoFe-Co@PNC-12. (b) The calculated free-energy diagrams of ORR and OER on the CoFe/Co-NC-12 and Co/Co-NC (U = 1.23 V). (c) The projected density of states (PDOS) on pristine Co nanoparticles, Fe in CoFe Alloy and Co in FeCo alloy. The spin charge density distribution of (d) CoFe@Co-NC and (e) Co@Co-NC (Top view), inset figure illustrates side view (blue color shows the charge losing and the yellow isosurface shows the electron gaining).

are greatly promoted, thus optimizing the reaction path and accelerating the ORR/OER reaction kinetics.

3.4 Rechargeable Zn-air battery test

Based on CoFe-Co@PNC-12 excellent ORR and OER bifunctional catalytic performance, a rechargeable liquid Zn–air battery was fabricated to evaluate its feasibility under real battery operating conditions (Fig. 5(a) and Fig. S23 in the ESM) [60]. As the reference, the device made of commercial Pt/C+RuO₂ as air electrode was tested under the same experimental conditions. As illustrated in Figs. 5(b) and 5(c), the ZABs based on CoFe-Co@PNC-12 provides an open circuit potential (OCP) of 1.45 V, greater than Pt/C + RuO₂ (1.43 V). The discharge polarization curve and the corresponding power density plots are shown in Fig. 5(d). The maximum power density of the ZABs fabricated with CoFe-Co@PNC-12 is 152.8 mW·cm⁻², significantly higher than Pt/C + RuO₂ catalyst (73 mW·cm⁻²). Moreover, after normalized to the amount of Zn, catalyst CoFe-Co@PNC-12 also show a high specific capacity of 786 and 762 mAh·g⁻¹ at 10 and 20 mA·cm⁻², respectively. The corresponding gravimetric energy density is up to 943 and 883 Wh·kg⁻¹ (Fig. 5(e)). The efficiency and long-term chargeability of CoFe-Co@PNC-12 of ZABs are characterized by galvanostatic charge-discharge at a current density of 10 mA·cm⁻². As shown in Fig. 5(f), the initial charge-discharge voltage gap of CoFe-Co@PNC-12 is 0.94 V, smaller than the Pt/C + RuO₂ catalyst (1.19 V). The ZABs assembled with

CoFe-Co@PNC-12 also is observed to has excellent durability without obvious voltage attenuation after more than 200 h of continuous charging and discharging process, while the battery using Pt/C + RuO₂ catalyst provides a poor cycling with operating time of less than 60 h. The excellent charge- discharge efficiency and stability of CoFe-Co@PNC-12 are mainly ascribed to its unique structure consist of hollow porous Co-N-doped Carbons embedded with ultrafine CoFe/Co Nanoparticles, providing fast mass transfer, and the inherent stability of CoFe alloy and Co-N sites. In addition, as shown in Fig. 5(g), three ZABs using CoFe-Co@PNC-12 as air electrode can be connected in series to light up an light emitting diode (LED) display (9 cm × 3 cm, 3.8 V), showing promising applications.

Encouraged by the increasing demand for portable and flexible electronic equipment, a solid state flexible ZABs (Fig. 6(a)) was prepared using the prepared CoFe-Co@PNC-12 as membrane cathode and PVA-KOH electrolyte [61]. Figure 6(b) shows that the battery can cycling charge-discharge smoothly at different bending angles without the change of voltage gaps. Moreover, solid ZABs also shows a very stable high OCP at different bending angles in Figs. 6(c) and 6(d). As an example of real device, the solid-state ZABs in series can power the timer for more than 1 h and operate well throughout the entire bending process (Fig. S24 in the ESM). These results indicate that our CoFe-Co@PNC-12 catalyst possess considerable potential in rechargeable flexible solid ZABs and wearable devices.
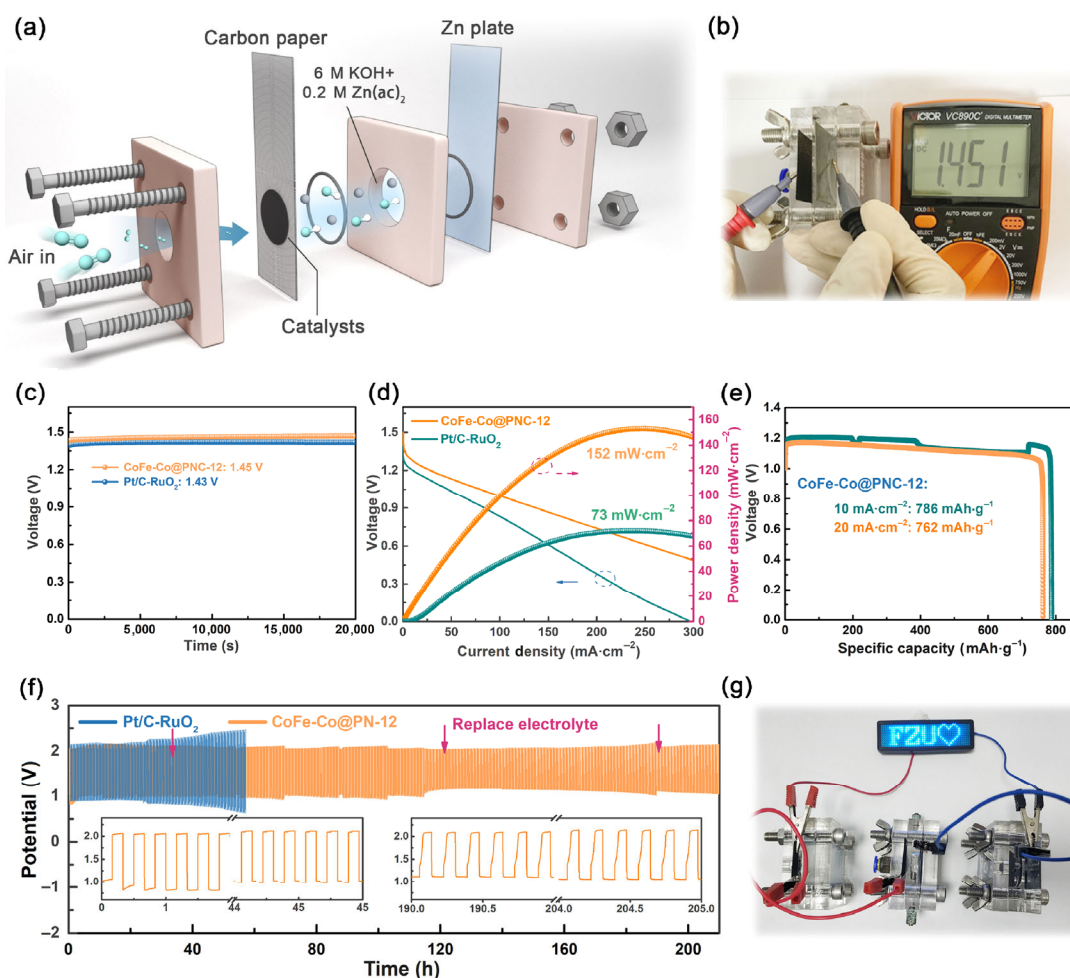

Figure 5 (a) Assembly diagram of rechargeable ZABs and OCV plot (b) and (c) with the inset showing a stable OCV of 1.45 V and (d) polarization and power density plots of ZABs. (e) Specific capacity curves of ZAB normalized with the Zn consumed using CoFe-Co@PNC-12 and Pt/C+RuO₂ as catalyst. (f) Galvanostatic cycling stability of CoFe-Co@PNC-12 and Pt/C+RuO₂ at 10 mA·cm⁻² with the inset shows charging and discharging at different cycle numbers. (g) Optical image of a LED panel lighted by three ZAB in series.
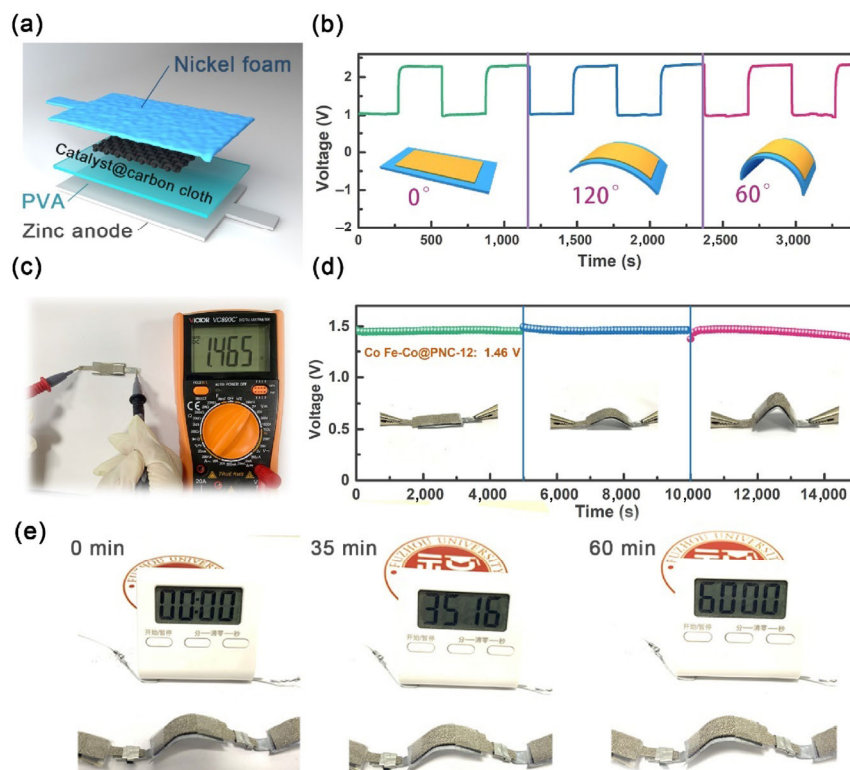
Figure 6 (a) Schematic illustration of flexible, solid-state ZAB. (b) Galvanostatic cycling stability of ZAB with CoFe-Co@PNC-12 as the cathode catalysts in different bending states at 10 mA·cm^{-2}. (c) Optical image of the ZAB affording a stable OCV of 1.46 V and (d) OCV plots and Power density plots. (e) Photograph of timer powered by three ZAB connected in series.

4 Conclusion

In summary, a core-shell structure of highly active bifunctional oxygen catalysts CoFe-Co@PNC-12 was synthesized through an improved silicon protection-iron infiltration strategy. The coated silicon shell not only effectively prevents the agglomeration of metal particles, but also promotes the formation of core-shell structure. The infiltration of Fe^{2+} formed CoFe alloy to solve the problem of poor active sites after acid etching. The unique core-shell structure and the synergistic effect between CoFe alloy and Co-N site further improve the oxygen catalytic activity. DFT calculation confirmed that the synergistic promotion effect between CoFe alloy and Co-N site effectively reduced the formation energy of from O* to OH*, thus further catalyzes ORR and OER. In view of such excellent structural characteristics, the optimized samples CoFe-Co@PNC-12 shows more efficient bifunctional oxygen catalytic activity than commercial Pt/C+RuO$_2$ catalysts when applied in the rechargeable liquid and flexible solid-state ZABs. This work provides a new strategy to develop MOF derived high performance of non-noble metal bifunctional electrocatalysts for next-generation flexible electronic devices.

References

[1] Li, Y. G.; Dai, H. J. Recent advances in zinc-air batteries. *Chem. Soc. Rev.* **2014**, *43*, 5257–5275.

[2] Meng, F. L.; Liu, K. H.; Zhang, Y.; Shi, M. M.; Zhang, X. B.; Yan, J. M.; Jiang, Q. Recent advances toward the rational design of efficient bifunctional air electrodes for rechargeable Zn-air batteries. *Small* **2018**, *14*, 1703843.

[3] Wu, M. J.; Zhang, G. X.; Wu, M. H.; Prakash, J.; Sun, S. H. Rational design of multifunctional air electrodes for rechargeable Zn–air batteries: Recent progress and future perspectives. *Energy Storage Mater.* **2019**, *21*, 253–286.

[4] Zhu, C. Y.; Ma, Y. Y.; Zang, W. J.; Guan, C.; Liu, X. M.; Pennycook, S. J.; Wang, J.; Huang, W. Conformal dispersed cobalt nanoparticles in hollow carbon nanotube arrays for flexible Zn-air and Al-air batteries. *Chem. Eng. J.* **2019**, *369*, 988–995.

[5] Fu, Y. Q.; Wei, Q. L.; Zhang, G. X.; Wang, X. M.; Zhang, J. H.; Hu, Y. F.; Wang, D. N.; Zuin, L.; Zhou, T.; Wu, Y. C. et al. High-performance reversible aqueous Zn-ion battery based on porous MnO$_x$ nanorods coated by MOF-derived N-doped carbon. *Adv. Energy Mater.* **2018**, *8*, 1801445.

[6] Liu, S. H.; Wang, Z. Y.; Zhou, S.; Yu, F. J.; Yu, M. Z.; Chiang, C. Y.; Zhou, W. Z.; Zhao, J. J.; Qiu, J. S. Metal-organic-framework-derived hybrid carbon nanocages as a bifunctional electrocatalyst for oxygen reduction and evolution. *Adv Mater.* **2017**, *29*, 1700874.

[7] Jin, H. H.; Zhou, H.; Ji, P. X.; Zhang, C. T.; Luo, J. H.; Zeng, W. H.; Hu, C. X.; He, D. P.; Mu, S. C. ZIF-8/LiFePO$_4$ derived Fe-N-P Co-doped carbon nanotube encapsulated Fe$_2$P nanoparticles for efficient oxygen reduction and Zn-air batteries. *Nano Res.* **2020**, *13*, 818–823.

[8] Zhang, J.; Huang, Q. A.; Wang, J.; Wang, J.; Zhang, J. J.; Zhao, Y. F. Supported dual-atom catalysts: Preparation, characterization, and potential applications. *Chin. J. Catal.* **2020**, *41*, 783–798.

[9] Cheng, H.; Li, M. L.; Su, C. Y.; Li, N.; Liu, Z. Q. Cu-Co bimetallic oxide quantum dot decorated nitrogen-doped carbon nanotubes: A high-efficiency bifunctional oxygen electrode for Zn-air batteries. *Adv. Func. Mater.* **2017**, *27*, 1701833.

[10] Wang, L.; Wang, Y. Q.; Wu, M. G.; Wei, Z. X.; Cui, C. Y.; Mao, M. L.; Zhang, J. T.; Han, X. P.; Liu, Q. H.; Ma, J. M. Nitrogen, fluorine, and boron ternary doped carbon fibers as cathode electrocatalysts for zinc-air batteries. *Small* **2018**, *14*, 1800737.

[11] Xu, Y. S.; Zhu, L. P.; Cui, X. X.; Zhao, M. Y.; Li, Y. L.; Chen, L. L.; Jiang, W. C.; Jiang, T.; Yang, S. G.; Wang, Y. Graphitizing N-doped mesoporous carbon nanospheres via facile single atom iron growth for highly efficient oxygen reduction reaction. *Nano Res.* **2020**, *13*, 752–758.

[12] Kong, F. T.; Qiao, Y.; Zhang, C. Q.; Fan, X. H.; Kong, A. G.; Shan, Y. K. Unadulterated carbon as robust multifunctional electrocatalyst for overall water splitting and oxygen transformation. *Nano Res.* **2020**, *13*, 401–411.

[13] Peng, H. L.; Liu, F. F.; Liu, X. J.; Liao, S. J.; You, C. H.; Tian, X. L.; Nan, H. X.; Luo, F.; Song, H. Y.; Fu, Z. Y. et al. Effect of transition metals on the structure and performance of the doped carbon catalysts derived from polyaniline and melamine for ORR application. *ACS Catal.* **2014**, *4*, 3797–3805.

[14] Wang, Z. High-efficiency bifunctional oxygen electrocatalysis. *Adv. Funct. Mater* **2019**, *29*, 1902875.

[15] Wei, Q. L.; Zhang, G. X.; Yang, X. H.; Fu, Y. Q.; Yang, G. H.; Chen, N.; Chen, W. F.; Sun, S. H. Litchi-like porous Fe/N/C spheres with atomically dispersed FeNx promoted by sulfur as highly efficient oxygen electrocatalysts for Zn–air batteries. *J. Mater. Chem. A* **2018**, *6*, 4605–4610.

[16] Wang, Y. J.; Fan, H. B.; Ignaszak, A.; Zhang, L.; Shao, S. Q.; Wilkinson, D. P.; Zhang, J. J. Compositing doped-carbon with metals, non-metals, metal oxides, metal nitrides and other materials to form bifunctional electrocatalysts to enhance metal-air battery oxygen reduction and evolution reactions. *Chem. Eng. J.* **2018**, *348*, 416–437.

[17] Sun, T. T.; Xu, L. B.; Wang, D. S.; Li, Y. D. Metal organic frameworks derived single atom catalysts for electrocatalytic energy conversion. *Nano Res.* **2019**, *12*, 2067–2080.

[18] Tang, C.; Wang, B.; Wang, H. F.; Zhang, Q. Defect engineering toward atomic Co-Nx-C in hierarchical graphene for rechargeable flexible solid Zn-air batteries. *Adv. Mater.* **2017**, *29*, 1703185.

[19] Wang, H. F.; Tang, C.; Zhang, Q. A review of precious-metal-free bifunctional oxygen electrocatalysts: Rational design and applications in Zn–air batteries. *Adv. Funct. Mater* **2018**, *28*, 1803329.

[20] Liu, D. X.; Wang, B.; Li, H. G.; Huang, S. F.; Liu, M. M.; Wang, J.; Wang, Q. J.; Zhang, J. J.; Zhao, Y. F. Distinguished Zn, Co-Nx-C-Sy active sites confined in dentric carbon for highly efficient oxygen reduction reaction and flexible Zn-air batteries. *Nano Energy* **2019**, *58*, 277–283.

[21] Lu, Z. Y.; Wang, B.; Hu, Y. F.; Liu, W.; Zhao, Y. F.; Yang, R. O; Li, Z. P.; Luo, J.; Chi, B.; Jiang, Z. et al. An isolated zinc-cobalt atomic pair for highly active and durable oxygen reduction. *Angew. Chem., Int. Ed.* **2019**, *58*, 2622–2626.

[22] Li, S.; Cheng, C.; Zhao, X. J.; Schmidt, J.; Thomas, A. Active salt/silica-templated 2D mesoporous FeCo-Nx-carbon as bifunctional oxygen electrodes for zinc-air batteries. *Angew. Chem., Int. Ed.* **2018**, *57*, 1856–1862.

[23] Fu, Y.; Yu, H. Y.; Jiang, C.; Zhang, T. H.; Zhan, R.; Li, X. W.; Li, J. F.; Tian, J. H.; Yang, R. NiCo alloy nanoparticles decorated on N-doped carbon nanofibers as highly active and durable oxygen electrocatalyst. *Adv. Funct. Mater.* **2018**, *28*, 1705094.

[24] Wan, W. J.; Liu, X. J.; Li, H. Y.; Peng, X. Y.; Xi, D. S.; Luo, J. 3D carbon framework-supported CoNi nanoparticles as bifunctional oxygen electrocatalyst for rechargeable Zn-air batteries. *Appl. Catal. B Environ.* **2019**, *240*, 193–200.

[25] Wu, K. L.; Chen, X.; Liu, S. J.; Pan, Y.; Cheong, W. C.; Zhu, W.; Cao, X.; Shen, R. G.; Chen, W. X.; Luo, J. et al. Porphyrin-like Fe-N4 sites with sulfur adjustment on hierarchical porous carbon for different rate-determining steps in oxygen reduction reaction. *Nano Res.* **2018**, *11*, 6260–6269.

[26] Wang, Y. Y.; Kumar, A.; Ma, M.; Jia, Y.; Wang, Y.; Zhang, Y.; Zhang, G. X.; Sun, X. M.; Yan, Z. F. Hierarchical peony-like FeCo-NC with conductive network and highly active sites as efficient electrocatalyst for rechargeable Zn-air battery. *Nano Res.* **2020**, *13*, 1090–1099.

[27] Sun, Y. L.; Wang, J.; Liu, Q.; Xia, M. R.; Tang, Y. F.; Gao, F. M.; Hou, Y. L.; Tse, J.; Zhao, Y. F. Itinerant ferromagnetic half metallic cobalt–iron couples: Promising bifunctional electrocatalysts for ORR and OER. *J. Mater. Chem. A* **2019**, *7*, 27175–27185.

[28] Zhong, X. W.; Yi, W. D.; Qu, Y. J.; Zhang, L. Z.; Bai, H. Y.; Zhu, Y. M.; Wan, J.; Chen, S.; Yang, M.; Huang, L. et al. Co single-atom anchored on Co3O4 and nitrogen-doped active carbon toward bifunctional catalyst for zinc-air batteries. *Appl. Catal. B Environ.* **2020**, *260*, 118188.

[29] Tao, L.; Lin, C. Y.; Dou, S.; Feng, S.; Chen, D. W.; Liu, D. D.; Huo, J.; Xia, Z. H.; Wang, S. Y. Creating coordinatively unsaturated metal sites in metal-organic-frameworks as efficient electrocatalysts for the oxygen evolution reaction: Insights into the active centers. *Nano Energy* **2017**, *41*, 417–425.

[30] Liu, Z. Q.; Cheng, H.; Li, N.; Ma, T. Y.; Su, Y. Z. ZnCo2O4 quantum dots anchored on nitrogen-doped carbon nanotubes as reversible oxygen reduction/evolution electrocatalysts. *Adv. Mater.* **2016**, *28*, 3777–3784.

[31] Cheng, N. Y.; Ren, L.; Xu, X.; Du, Y.; Dou, S. X. Recent development of zeolitic imidazolate frameworks (ZIFs) derived porous carbon based materials as electrocatalysts. *Adv. Energy Mater.* **2018**, *8*, 1801257.

[32] Li, Y. L.; Jia, B. M.; Fan, Y. Z.; Zhu, K. L.; Li, G. Q.; Su, C. Y. Bimetallic zeolitic imidazolite framework derived carbon nanotubes embedded with Co nanoparticles for efficient bifunctional oxygen electrocatalyst. *Adv. Energy Mater.* **2018**, *8*, 1702048.

[33] Sultan, S.; Tiwari, J. N.; Jang, J. H.; Harzandi, A. M.; Salehnia, F.; Yoo, S. J.; Kim, K. S. Highly efficient oxygen reduction reaction activity of graphitic tube encapsulating nitrided CoxFey alloy. *Adv. Energy Mater.* **2018**, *8*, 1801002.

[34] Shang, L.; Yu, H. J.; Huang, X.; Bian, T.; Shi, R.; Zhao, Y. F.; Waterhouse, G. I. N.; Wu, L. Z.; Tung, C. H.; Zhang, T. R. Well-dispersed ZIF-derived Co, N-Co-doped carbon nanoframes through mesoporous-silica-protected calcination as efficient oxygen reduction electrocatalysts. *Adv. Mater.* **2016**, *28*, 1668–1674.

[35] Xia, W.; Zou, R. Q.; An, L.; Xia, D. G.; Guo, S. J. A metal–organic framework route to *in situ* encapsulation of Co@Co3O4@C core@bishell nanoparticles into a highly ordered porous carbon matrix for oxygen reduction. *Energy Environ. Sci.* **2015**, *8*, 568–576.

[36] Wang, C. H.; Kim, J.; Tang, J.; Kim, M.; Lim, H.; Malgras, V.; You, J.; Xu, Q.; Li, J. S.; Yamauchi, Y. New strategies for novel MOF-derived carbon materials based on nanoarchitectures. *Chem* **2020**, *6*, 19–40.

[37] Zhou, H.; He, D. P.; Saana, A. I.; Yang, J. L.; Wang, Z.; Zhang, J.; Liang, Q. R.; Yuan, S.; Zhu, J. W.; Mu, S. C. Mesoporous-silica induced doped carbon nanotube growth from metal-organic frameworks. *Nanoscale* **2018**, *10*, 6147–6154.

[38] Sa, Y. J.; Seo, D. J.; Woo, J.; Lim, J. T.; Cheon, J. Y.; Yang, S. Y.; Lee, J. M.; Kang, D.; Shin, T. J.; Shin, H. S. et al. A general approach to preferential formation of active Fe-Nx sites in Fe-N/C electrocatalysts for efficient oxygen reduction reaction. *J. Am. Chem. Soc.* **2016**, *138*, 15046–15056.

[39] Hu, B. C.; Wu, Z. Y.; Chu, S. Q.; Zhu, H. W.; Liang, H. W.; Zhang, J.; Yu, S. H. SiO2-protected shell mediated templating synthesis of Fe–N-doped carbon nanofibers and their enhanced oxygen reduction reaction performance. *Energy Environ. Sci.* **2018**, *11*, 2208–2215.

[40] Gao, C. B.; Zhang, Q.; Lu, Z. D.; Yin, Y. D. Templated synthesis of metal nanorods in silica nanotubes. *J. Am. Chem. Soc.* **2011**, *133*, 19706–19709.

[41] Liu, C.; Huang, X. D.; Wang, J,; Song, H.; Yang, Y. N.; Liu, Y.; Li, J. S.; Wang, L. J.; Yu, C. Z. Hollow mesoporous carbon nanocubes: Rigid-interface-induced outward contraction of metal-organic frameworks. *Adv. Funct. Mater.* **2017**, *28*, 1705253.

[42] Tang, C.; Wang, H. F.; Chen, X.; Li, B. Q.; Hou, T. Z.; Zhang, B. S.; Zhang, Q.; Titirici, M. M.; Wei, F. Topological defects in metal-free nanocarbon for oxygen electrocatalysis. *Adv. Mater.* **2016**, *28*, 6845–6851.

[43] Ito, Y.; Cong, W. T.; Fujita, T.; Tang, Z.; Chen, M. W. High catalytic activity of nitrogen and sulfur co-doped nanoporous graphene in the hydrogen evolution reaction. *Angew. Chem., Int. Ed.* **2015**, *54*, 2131–2136.

[44] Chen, L. L.; Zhang, Y. L.; Liu, X. J.; Long, L.; Wang, S. Y.; Xu, X. L.; Liu, M. C.; Yang, W. X.; Jia, J. B. Bifunctional oxygen electrodes of homogeneous Co_4N nanocrystals@N-doped carbon hybrids for rechargeable Zn-air batteries. *Carbon* **2019**, *151*, 10–17.

[45] Su, C. Y.; Cheng, H.; Li, W.; Liu, Z. Q.; Li, N.; Hou, Z. F.; Bai, F. Q.; Zhang, H. X.; Ma, T. Y. Atomic modulation of FeCo-nitrogen-carbon bifunctional oxygen electrodes for rechargeable and flexible all-solid-state zinc-air battery. *Adv. Energy Mater.* **2017**, *7*, 1602420.

[46] Fang, W. G.; Hu, H. B.; Jiang, T. T.; Li, G.; Wu, M. Z. N- and S-doped porous carbon decorated with *in-situ* synthesized Co–Ni bimetallic sulfides particles: A cathode catalyst of rechargeable Zn-air batteries. *Carbon* **2019**, *146*, 476–485.

[47] Ali-Löytty, H.; Louie, M. W.; Singh, M. R.; Li, L.; Casalongue, H. G. S.; Ogasawara, H.; Crumlin, E. J.; Liu, Z.; Bell, A. T.; Nilsson, A. et al. Ambient-pressure XPS study of a Ni–Fe electrocatalyst for the oxygen evolution reaction. *J. Phys. Chem. C* **2016**, *120*, 2247–2253.

[48] Wu, W. T.; Zhang, Q. G.; Wang, X. K.; Han, C. C.; Shao, X. D.; Wang, Y. X.; Liu, J. L.; Li, Z. T.; Lu, X. Q.; Wu, M. B. Enhancing selective photooxidation through Co–N_x-doped carbon materials as singlet oxygen photosensitizers. *ACS Catal.* **2017**, *7*, 7267–7273.

[49] Luo, E. G.; Zhang, H.; Wang, X.; Gao, L. Q.; Gong, L. Y.; Zhao, T.; Jin, Z.; Ge, J. J.; Jiang, Z.; Liu, C. P. et al. Single-atom Cr-N_4 sites designed for durable oxygen reduction catalysis in acid media. *Angew. Chem., Int. Ed.* **2019**, *58*, 12469–12475.

[50] Liao, K. M.; Mao, P.; Li, N.; Han, M.; Yi, J.; He, P.; Sun, Y.; Zhou, H. S. Stabilization of polysulfides via lithium bonds for Li–S batteries. *J. Mater. Chem. A* **2016**, *4*, 5406–5409.

[51] Lu, Q.; Yu, J.; Zou, X. H.; Liao, K. M.; Tan, P.; Zhou, W.; Ni, M.; Shao, Z. P. Self-catalyzed growth of Co, N-codoped CNTs on carbon-encased CoS_x surface: A noble-metal-free bifunctional oxygen electrocatalyst for flexible solid Zn-air batteries. *Adv. Funct. Mater.* **2019**, *29*, 1904481.

[52] Guo, D. H.; Shibuya, R.; Akiba, C.; Saji, S.; Kondo, T.; Nakamura, J. Active sites of nitrogen-doped carbon materials for oxygen reduction reaction clarified using model catalysts. *Science* **2016**, *351*, 361–365.

[53] Zhou, M.; Wang, H. L.; Guo, S. J. Towards high-efficiency nano-electrocatalysts for oxygen reduction through engineering advanced carbon nanomaterials. *Chem. Soc. Rev.* **2016**, *45*, 1273–1307.

[54] Wang, S. G.; Qin, J. W.; Meng, T.; Cao, M. H. Metal–organic framework-induced construction of actiniae-like carbon nanotube assembly as advanced multifunctional electrocatalysts for overall water splitting and Zn-air batteries. *Nano Energy* **2017**, *39*, 626–638.

[55] Zhou, R. F.; Zheng, Y.; Jaroniec, M.; Qiao, S. Z. Determination of the electron transfer number for the oxygen reduction reaction: From theory to experiment. *ACS Catal.* **2016**, *6*, 4720–4728.

[56] Wang, J.; Xin, H. L.; Zhu, J.; Liu, S. F.; Wu, Z. X.; Wang, D. L. 3D hollow structured Co_2FeO_4/MWCNT as an efficient non-precious metal electrocatalyst for oxygen reduction reaction. *J. Mater. Chem. A* **2015**, *3*, 1601–1608.

[57] Suntivich, J.; Gasteiger, H. A.; Yabuuchi, N.; Nakanishi, H.; Goodenough, J. B.; Shao-Horn, Y. Design principles for oxygen-reduction activity on perovskite oxide catalysts for fuel cells and metal-air batteries. *Nat. Chem.* **2011**, *3*, 546–550.

[58] Ling, T.; Yan, D. Y.; Jiao, Y.; Wang, H.; Zheng, Y.; Zheng, X. L.; Mao, J.; Du, X. W.; Hu, Z. P.; Jaroniec, M.; Qiao, S. Z. Engineering surface atomic structure of single-crystal cobalt (II) oxide nanorods for superior electrocatalysis. *Nat. Commun.* **2016**, *7*, 12876.

[59] Wang, X. R.; Liu, J. Y.; Liu, Z. W.; Wang, W. C.; Luo, J.; Han, X. P.; Du, X. W.; Qiao, S. Z.; Yang, J. Identifying the key role of pyridinic-N-Co bonding in synergistic electrocatalysis for reversible ORR/OER. *Adv. Mater.* **2018**, *30*, 1800005.

[60] Chen, X. C.; Zhou, Z.; Karahan, H. E.; Shao, Q.; Wei, L.; Chen, Y. Recent advances in materials and design of electrochemically rechargeable zinc-air batteries. *Small* **2018**, *14*, 1801929.

[61] Yang, D.; Tan, H. T.; Rui, X. H.; Yu, Y. Electrode materials for rechargeable zinc-ion and zinc-air batteries: Current status and future perspectives. *Electrochem. Energy Rev.* **2019**, *2*, 395–427.